Strain energy density of VO₂-based microactuators

Emmanuelle Merced*, Xiaobo Tan, Nelson Sepúlveda

Applied Materials Group, Department of Electrical and Computer Engineering, Michigan State University, East Lansing, MI 48824, United States

ARTICLE INFO

ABSTRACT

The strain, stress and strain energy density of a vanadium dioxide (VO₂)-based microactuator were obtained from experimental curvature measurements as a function of temperature. The study revealed fully reversible strain and stress changes of up to -0.32% and -510 MPa, respectively, and a maximum strain energy density of approximately 8.1×10^5 J/m³ through a temperature window of only 15 °C. The method for obtaining the strain energy density in this work is more accurate than the ones presented previously in the literature. The obtained values were validated with a temperature-dependent solid mechanics finite element analysis simulation. Microactuator performance was also studied inside its hysteretic region through a series of heating and cooling cycles, providing a more complete performance analysis of the device properties.

1. Introduction

Micromechanical actuators are devices with micrometer dimensions that can convert one type of energy or signal into another. In many cases, the output signal of an actuator is the displacement or force of a suspended structure (e.g. cantilever, membrane, rotating gear) [1–19]. They are characterized by the amount of work that they can perform, and can be classified according to the type of energy or signal they receive and how they convert it. There are different actuation methods that have been used successfully, such as magnetic [1,2], piezoelectric [3,20,21], electrostatic [4–9], and thermal [11–16]; all of which have their advantages, limitations, and trade-offs.

Typically, electromagnetic and magnetostatic actuators have low output forces and displacements. This is due to the fact that the forces induced by magnetic fields scale down very rapidly with size. Currents of 80 mA have generated 200 μN of actuation force and bending displacements of 50 μm [1]. The size of that device was about 8 mm². Five years later, a spiral-type magnetic microactuator was capable of producing displacements up to 28 μm and produce forces of 1.24 mN [2]. However, this device – and the spiral actuator reported a year earlier [22] – had dimensions in the millimeter range. Electromagnetic and magnetostatic actuators usually need an excitation source external to the chip where the device is located,

making difficult if not impossible their integration into one single chip. On the other hand, mechanically amplified piezoelectric actuators can provide displacements up to 1.2 mm [3]. Nevertheless, piezoelectric actuators that can provide such large displacements also have dimensions in the millimeter range.

Micrometer sized electrostatic actuators use the attractive (or repelling) force between two charged plates or surfaces. When they are fabricated in the micrometer scale, they can sustain very high electric fields since the gaps between the charged surfaces can be smaller than the mean free path of particles in air at room temperature (approximately 6 μm). Electrostatic comb-drives have been actuated with 20 V and achieved displacements close to 30 μm [4]. Later improvements in the design and fabrication led to displacements of up to 150 μm in 1 ms on comb-drive devices actuated with 150 V [5]. Comb-drives are usually the type of devices used for actuating micro engines. Although relatively large torques have been delivered, because the gear movement is rotational (angular motion), the linear displacements have been close to 40 μm [6]. However, other types of electrostatic actuators, such as scratch drives and impact actuators, can be used to obtain deflections as large as 200 μm [7]. Impact actuators need multiple motions (or impacts) in order to get a total displacement in the micrometer range. For example, an AC voltage signal with amplitude of 100 V and frequency of 200 Hz was applied to an impact microactuator for 500 ms and a displacement of 1.35 μm was obtained [8]. The dimensions of this device were 3 mm × 3 mm × 600 μm. The device was tested for over 550 cycles on a fixed sample and survived without any deterioration. Scratch drive actuators are also usually operated by an AC voltage and can supply forces close to 1 mN and have displacements close to 200 μm [9].

* Corresponding author at: Applied Materials Group, Department of Electrical and Computer Engineering, Michigan State University, 2120 Engineering Building, East Lansing, MI 48824, United States. Tel.: +1 517 355 7523; fax: +1 517 353 1980.
  E-mail address: mercedem@msu.edu (E. Merced).

The *family* of thermal actuators can be divided according to the phenomenon caused by the difference in temperature. Among all the types of mechanical actuators, shape memory alloy (SMA) actuators offer the highest strain energy density [7]. They have been used to develop wireless bio-mimicking micro-robots [10]. However, their dimensions are in the millimeter range and the reported displacements are not larger than 35 μm [11]. Thermopneumatic actuation can be achieved by changing the pressure level inside a cavity using a heater electrode that moves the sealing diaphragm. A corrugated silicon diaphragm (which is more flexible than a flat one) was driven by thermopneumatic actuation and the maximum displacement was 40 μm [12]. The third subclass of thermal actuators uses thermal expansion mechanisms. Thermal expansion actuators are basically released structures (e.g. cantilevers) made out of at least two different materials with different thermal expansion coefficients. When heated, the difference in the thermal expansion coefficients causes both layers to expand at different rates. This produces a cantilever bending in a direction perpendicular to both films, with the film with the lowest thermal expansion coefficient facing the inner side of the arc formed by the cantilever. The largest displacements that have been observed with this type of actuators use some type of polymer as one of the materials that form the bilayer cantilever. Polyimide based bilayered cantilevers have shown impressive bending capabilities [13]. However, once again, the dimensions of these cantilevers are in the millimeter range. Other smaller cantilevers (300 μm long) have also been coated with polymers to obtain deflections up to 50 μm [14]. The use of polymers limits the use of such cantilevers for temperatures below their melting temperature (approximately 400 °C). Finite element methods have been used to optimize the actuator geometry for maximum deflections on thermal actuators about 150 μm long and 50 μm wide, but no deflections larger than 20 μm were obtained [15,16].

More recently, researchers have found that smart materials – such as electroactive polymers and phase change materials – provide new actuation mechanisms capable of performing beyond the theoretical limits of the technologies mentioned above. Electroactive polymers have demonstrated good performance in air [17] and liquid [18] environments, which makes them suitable for biomedical applications. They also operate at very low power with highest strain energy density in the vicinity of 5×10^4 J/m^3 [19].

Strain energy density is perhaps the most important figure of merit used to describe the performance of a micro-actuator, since it normalizes the device work capacity with respect to size. Response time, repeatability, and memory capability are other significant parameters used for describing the device behavior; whereas the potential applications of such devices is also influenced by other factors like the energy and method required for actuation.

This paper describes the advantages of incorporating thin films of a phase change material – vanadium dioxide (VO$_2$) – in microcantilevers used as actuators. When a microcantilever is coated with a VO$_2$ thin film, the abrupt change in the crystallographic structure of VO$_2$ across its solid-solid phase change could cause drastic deflections in the bilayered system (depending on the film orientation). Although this phenomenon has been described in detail previously [22] – together with its programmable and repeatable capability [23] – the strain energy density has never been addressed. The potential use of these devices in multiple microactuator applications was unveiled recently by their completely reversible behavior with no degradation in bending amplitude up to frequencies of 1 kHz when photothermally actuated in air (10 Hz when actuated in water) [24]. Such potential is confirmed in this paper, which demonstrates that they are also capable of providing strain energy densities close to those of the highest values reported so far using other technologies.

In this work, the strain developed during the phase change of the VO$_2$-film deposited on a single crystal silicon (SCS) cantilever was experimentally measured and used to calculate (analytically) the stress in the bilayered cantilever. Using these two values, the strain energy density was obtained. The mathematical approach and analysis used in this paper does not rely on small-angle or one-layer approximations, and therefore provides a much more accurate value for strain energy densities of VO$_2$-based microactuators than estimates done in the past [22]. The experimental and analytical results were verified using numerical simulations, which have not been done previously for any type of VO$_2$ microactuators. The evolution of strain, stress and strain energy density as a function of temperature throughout the VO$_2$ transition is also studied, which is important for modeling and control purposes.

2. Experimental procedure

2.1. Sample preparation

VO$_2$ was deposited by pulsed laser deposition on a SCS microcantilever with length, width and thickness of 300, 35 and 1 μm, respectively. The SCS crystallographic plane parallel to the cantilever surface corresponded to the (1 0 0), where high quality VO$_2$ has been deposited in the past [22,25]. The deposition was performed in a vacuum chamber at a pressure of 20 mTorr with a background pressure of approximately 10^{-6} Torr. An oxygen and argon atmosphere was maintained with gas flows of 15 and 10 standard cubic centimeter per minute (sccm), respectively. Although the sample temperature was not directly measured throughout the deposition time of 30 min, a substrate-to-controller temperature calibration was conducted before the deposition. From this calibration, the approximate substrate deposition temperature was approximately 550 °C. A krypton fluoride excimer laser (Lambda Physik LPX 200, λ = 248 nm) was focused on a rotating vanadium target with an intensity of 350 mJ at a repetition rate of 10 pulses per second. The sample was positioned 0.5 in. away from the heater and facing the target at a distance of 2.5 in. The sample was constantly rotated through the deposition in order to ensure a uniform temperature and thickness distribution. The thickness of the VO$_2$ layer was 172 nm, as measured by a profilometer on a Si test substrate to which the sample was attached during deposition. Fig. 1 shows the microactuator cross-section after the VO$_2$ deposition and the scanning electron microscopy (SEM) photo of the device.

2.2. Film characterization

The test substrate, which also contained VO$_2$, was used for electrical resistance characterization purposes. The test piece was placed on top of a Peltier heater in a 4-point probe (Signatone, S-301-4) and two of its electrical terminals were connected to a multimeter (Keithley, 2400). The temperature of the heater was measured with a monolithic integrated circuit temperature transducer (AD592) and controlled in closed-loop with a benchtop temperature controller (Thorlabs, TED4015). Fig. 2 shows the VO$_2$ film resistance as a function of temperature through a heating–cooling cycle from 30 to 100 °C in steps of 0.5 °C. For each setpoint, the measurements were performed after 4 s of reaching steady-state temperature value. This hold time value was empirically found to be optimal in the trade-off between temperature settling time and experiment duration. The same hold time was used for all the experiments presented here. A transition temperature of approximately 68 °C can be noticed. The curve follows
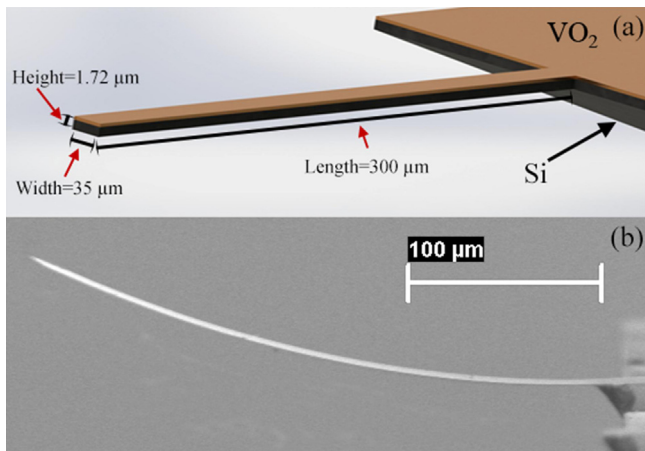
Fig. 1. Microactuator device diagram after VO$_2$ deposition in microcantilever (a) and SEM picture of the finalized device (b). The height in the diagram corresponds to the total thickness of the silicon and the VO$_2$ layers. The observed post-deposition bending is due to the residual film stress.
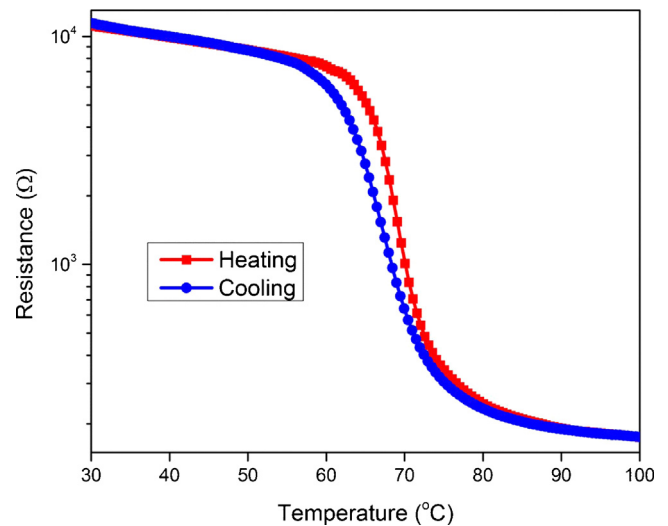

Fig. 2. Resistance as a function of temperature of the VO$_2$ thin film deposited on (1 0 0) silicon.

the abrupt drop in resistance and exhibits pronounced hysteretic behavior as observed in previous work for VO$_2$ deposited on (1 0 0)-oriented SCS structures [26].

The VO$_2$ thin film was also characterized by its structural change across the phase transition. The inset picture in Fig. 3 is a superimposed scanning electron microscopy (SEM) photo of the VO$_2$-coated SCS cantilever at 30 and 70 °C, which shows the characteristic large deflections of the bi-layered structure due to the phase transition [22,25,26]. Section 3 presents a detailed explanation of the thermal mechanisms that drive the microactuator.

2.3. Measurement setup

The VO$_2$-coated Si microactuator was placed in the setup shown in Fig. 3 in order to measure its tip deflection change through heating–cooling cycles between 21 °C and 84 °C. The microactuator chip was glued with a highly thermally conductive silver paint to a silicon substrate which was then placed on a Peltier heater. The silicon substrate's only purpose was to hold the microactuator chip during the experiments. The temperature of the heater was controlled in closed loop using the same benchtop temperature controller (TC) and sensor (TS) used for the resistance measurements in Fig. 2. The cantilever deflection was measured by using the

reflection of an infra-red (IR) laser (λ = 808 nm, rated at a maximum of 20 mW) aimed at the tip of the microactuator. The reflected light beam was then focused to the active area of a one-dimensional position sensitive detector (PSD, Hamamatsu S3270). The intensity of the sensing IR laser was kept at the minimum possible for reducing laser self-heating while maximizing the signal to noise ratio.

The bending of the bilayer microactuator was monitored by the displacement of the sensing IR laser beam incident on the PSD, which changed its output voltage. The PSD voltage was measured by an embedded real-time controller (NI cRIO 9075) with an analog input module (NI 9201). For alignment purposes, two charge-coupled device (CCD) cameras were used; one of them provided top view alignment of the sensing laser (CCD1) while the other provided a side view of the microactuator (CCD2) through an objective lens that magnified the image. Images obtained from the microactuator sideview were used to calibrate the output voltage from the PSD into microactuator tip deflection. A LabView program was developed to automatize the tip deflection measurements of the bilayer microactuator as a function of temperature. In this program, an arbitrary temperature sequence could be programmed into the cRIO controller. The cRIO acted as a supervisory controller, which communicated the temperature setpoint from the input sequence to the temperature controller while
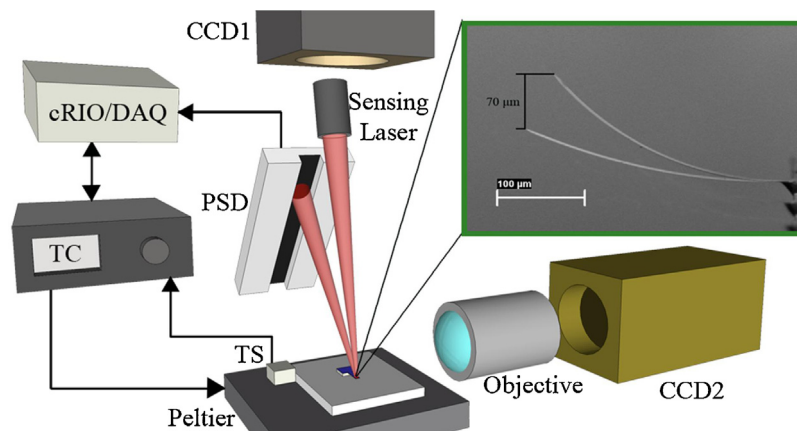

Fig. 3. Setup used for the temperature-dependent microactuator tip displacement measurements. The inset is an SEM picture of the microactuator sideview, which shows large tip displacements under temperature change.
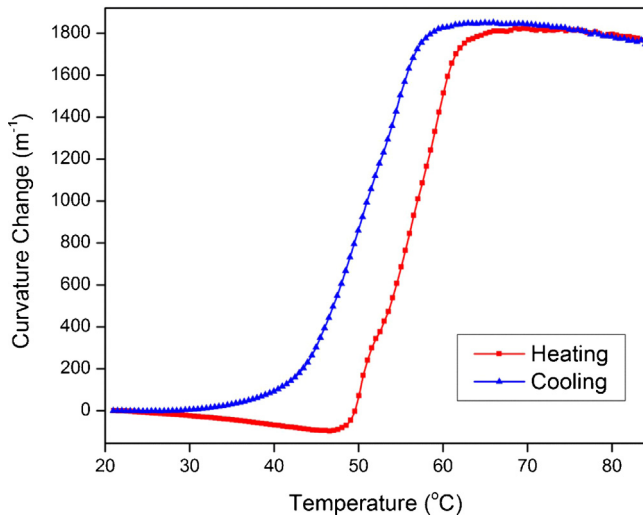
Fig. 4. Experimental measurement of microactuator curvature change as a function of temperature through a complete heating and cooling cycle (21–84 °C).
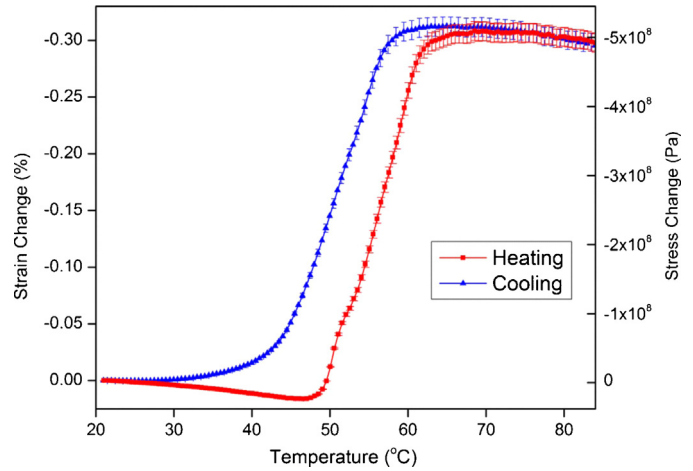

Fig. 5. Microactuator strain and stress change as a function of temperature through the complete heating and cooling cycle (21–84 °C). The error bars (±2.6%) correspond to the strain error due to the uncertainty of the biaxial modulus of the VO$_2$ layer. The error produced on the stress values is much less (±0.2%) and is not shown for clarity.

3. Results and discussion

3.1. Curvature change

The measured tip displacement of the microcantilever was used to calculate the curvature (k) from the transcendental equation given by

$$\Delta z = \frac{2}{k} \sin^2 \left(\frac{kL}{2} \right), \tag{1}$$

where Δz is the tip deflection change and L is the length of the microactuator. Since the microactuator in this work showed large initial deflection (see inset in Fig. 3), this Δz corresponds to the deflection change relative to the initial deflection at room temperature. The initial value measured was 67 μm. Fig. 4 shows the curvature change (relative to the initial curvature) as a function of temperature in steps of 0.5 °C, calculated from Eq. (1). A maximum curvature change of approximately 1800 m^{-1} was observed through the VO$_2$ phase transition.

The curvature change follows a non-monotonic behavior as a function of temperature, which is briefly explained. The thermal expansion coefficient of Si at room temperature (2.6×10^{-6} K^{-1}) [27] is smaller than the average coefficient of VO$_2$ (5.7×10^{-6} K^{-1}) [28], meaning that for increasing temperatures, the change in curvature due to differential thermal expansion will be negative and linear. This is what is observed in Fig. 4 for temperatures less than 30 °C and above 70 °C. However, as the temperature increases into the transition region, the VO$_2$ crystallographic plane parallel to the surface of the SCS cantilever shrinks, producing a compressive stress that bends the cantilever upward (positive curvature change) [22]. Thus, the observed curvature change is produced by two competing mechanisms: (1) the differential thermal expansion from both materials (dominant mechanism outside the phase transition) and (2) the abrupt built up of compressive stress produced by the VO$_2$ layer as the material undergoes its phase transition (dominant mechanism during the phase transition). This process is fully reversible. In the past, photothermal actuation of similar structures has shown no amplitude reduction or degradation up to hundreds of thousands of cycles [25].

3.2. Strain and stress changes

In order to find the stress and strain produced by the microactuator due to the phase transition of the VO$_2$, including the effect of the thermal expansion between the two layers, the following mathematical treatment was employed. The relationship between the bilayer microactuator curvature and strain is given by [29]

$$\varepsilon_T = \frac{E_f^2 H_f^4 + E_s^2 H_s^4 + 2E_f E_s H_f H_s(2H_f^2 + 2H_s^4 + 3H_f H_s)}{6H_f E_s H_f H_s(H_f + H_s)}k, \tag{2}$$

where the subscripts f and s are for the film and substrate parameters, respectively, E is the biaxial modulus, H is the thickness, k is the curvature and ε_T is the thermal strain. For the particular case of the VO$_2$ microactuator studied here, the total thermal strain is defined as the sum of the strains produced by: (1) the difference in thermal expansion coefficients from the two layers and (2) a hysteretic nonlinear term that represents the strain generated by the phase transition of the VO$_2$ layer. Since the thickness of the two layers are known, ε_T can be calculated from Eq. (2) for every temperature value, by assuming the silicon biaxial modulus in the (1 0 0) direction, E_s = 180.5 GPa [30] and the biaxial modulus of VO$_2$, E_f = 156 GPa. Although the used value for VO$_2$ is an average of the values found in literature [31–33], an error of up to 10 percent was taken into consideration in all calculations. The strain change of the microactuator throughout the major heating–cooling loop is shown in Fig. 5. A total strain change of −0.32% (where the negative denotes compression) was obtained with a strain change rate of −0.022% per °C through the VO$_2$ transition, which is in accordance with the previously obtained results [22]. A maximum error of ±2.6% was obtained with the deviation of the VO$_2$ biaxial modulus. This strain change produces an axial thermal stress (σ_T), which can be calculated from [29]

$$\sigma_T = \frac{E_f E_s(H_f + H_s)(E_s H_s^2(3H_f + H_s) + E_f H_f^2(H_f + 3H_s))}{E_f^2 + H_f^4 + E_s^2 H_s^4 + 2E_f E_s H_f H_s(2H_f^2 + 2H_s^4 + 3H_f H_s)}\varepsilon_T. \tag{3}$$

Fig. 5 also shows the thermal stress change as a function of temperature for the same major heating–cooling loop. A maximum error of ±0.2% is obtained when considering the VO$_2$ biaxial modulus variations. A recoverable stress of −510 MPa was obtained from the results of Eq. (3) (stress change rate of −36 MPa/°C through the material's transition), which is higher than the −379 MPa obtained by wafer curvature measurements of VO$_2$ deposited on Si reported
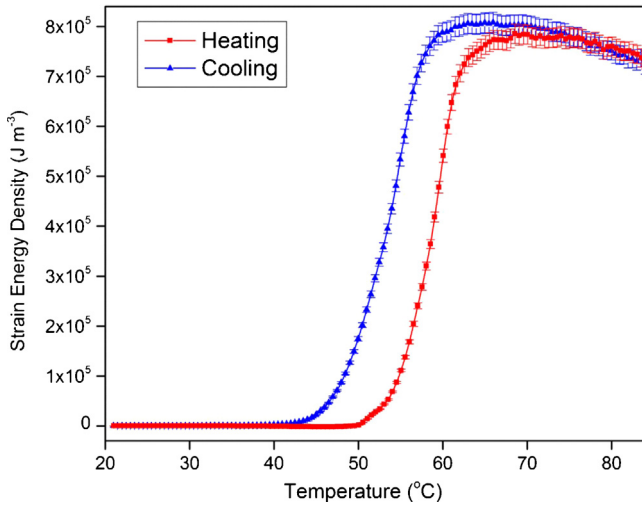
Fig. 6. Microactuator strain energy density as a function of temperature through the complete heating and cooling cycle (21–84 °C). The error bars represent the ±2.4% error due to the uncertainty of the biaxial modulus of the VO_2.

by Viswanath et al. [34]. In another work, the stress produced by the material's transition was estimated from cantilever curvature changes using a modified version of Stoney's equation [22]. A value of approximately 1 GPa was estimated, which is about twice the value reported here. However, since the Stoney's equation used to estimate this value assumes infinitesimal deflection (small angle approximation) the 1 GPa value is likely to be an overestimate of the real value. Hence, the analytical study presented in this work is believed to result in a more accurate representation of the reversible stress produced in VO_2-coated silicon microactuator.

3.3. Strain energy density

The strain energy density (W) of a bilayer microactuator made of isotropic materials is defined by [35]

$$W = \frac{1}{2}\sigma\varepsilon, \qquad (4)$$

where σ and ε are the produced stress and strain, respectively. For the case of the microactuator presented in this work, the stress and strain values were those obtained from Eqs. (2) and (3) for each of the temperature values measured. After substituting Eqs. (2) and (3) on Eq. (4) the strain energy density can be expressed in terms of the curvature, biaxial elastic moduli, and thicknesses:

$$W = \frac{(E_s H_s^2(3H_f + H_s) + E_f H_f^2(H_f + 3H_s))(E_f^2 H_f^4 + E_s^2 H_s^4 + 2E_f E_s H_f H_s(2H_f^2 + 2H_s^4 + 3H_f H_s))}{36 E_f E_s H_f^2 H_s^2 (H_f + H_s)} k^2. \qquad (5)$$

Fig. 6 shows the strain energy density induced by the device through the major heating–cooling loop calculated from Eq. (5). A strain energy density change of approximately 8.1×10^5 J/m³ was produced by the VO_2-based microactuator with a maximum deviation error of ±2.4% (due to the VO_2 biaxial modulus uncertainty) through a temperature window of only 15 °C. The strain energy density change rate throughout the transition is constantly increasing due to the squared curvature term in Eq. (5). As the phase transition ends, the difference in thermal expansion coefficient between the VO_2 and the SCS begins to become the dominant actuation mechanism, and the energy density change rate begins to decrease, also following a parabolic behavior.

Krulevitch et al. compared the strain energy density of various types of microactuators [11], all of which are shown in Fig. 7 along with that of VO_2-based microactuator studied in this paper. The strain energy density values are calculated from the
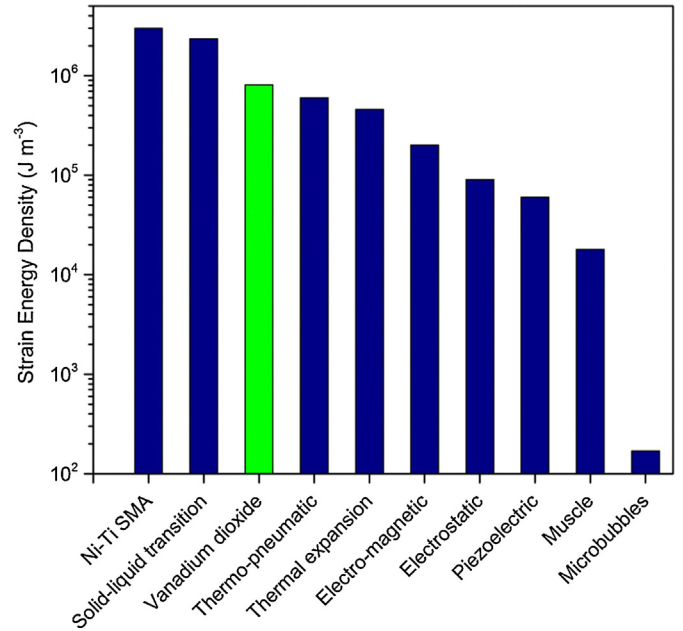

Fig. 7. Strain energy densities of different microactuators including the VO_2-based microactuator studied in this paper (green). The actuation mechanism for each microactuator can be found in the referenced work [11]. (For interpretation of the references to color in this figure legend, the reader is referred to the web version of the article.)

product of stress and strain divided by two (according to Eq. (4)). Although the VO_2-based microactuator does not have the highest value, it encompasses some other advantages. Firstly, the phase transition of the VO_2 transition is fully reversible, (which means that the microactuator will return to its original state after a complete actuation cycle), and they have been operated hundreds of thousands of cycles without showing degradation in the amplitude of deflection. In comparison, shape memory alloys (SMA) are not fully reversible and start fatiguing after less than a hundred cycles [11]. This means that the strain energy density of the SMA microactuator decays rapidly as the number of cycles increases. Secondly, VO_2-based microactuators are simple structures, easy and relatively inexpensive to fabricate, with demonstrated photothermal responses of fractions of milliseconds [25]. The fabrication of thermo-pneumatic microactuators is a very complicated process and its actuation usually involves very high

temperatures (around 300 °C) and slow transients (in the range of seconds) [36]. Solid–liquid phase transition based microactuators are also complicated structures and are mainly used for microfluidic applications, making difficult a fair technological comparison [37]. Finally, the reported strain energy density measured for VO_2-based microcantilevers in this paper is produced by a temperature difference of only 15 °C, whereas thermal expansion-based cantilevers require large temperature variations (>200 °C) in order produce a strain energy density comparable to that of VO_2-based cantilevers [38].

3.4. Numerical validation

In order to validate the calculated values from Eqs. (1)–(5) a numerical simulation was performed using the solid mechanics
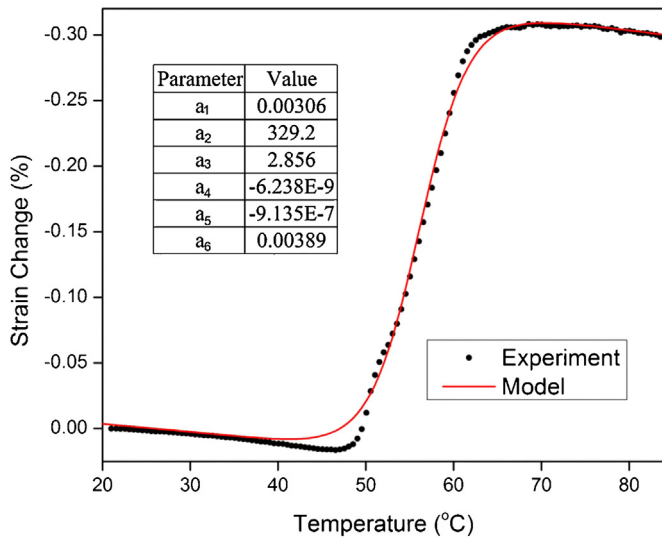
Fig. 8. Experimental strain change produced by the VO$_2$ phase transition (dots) and modified Boltzmann model (line) as a function of temperature. The inset table show the model parameters fitted by the experimental values.

Fig. 10. Experimental (dots) and simulated (line) strain energy density as a function of temperature.

module from the finite element analysis software, COMSOL Multiphysics. The thermal expansion and phase transition effects were considered in the model as to replicate the experimental procedure and find agreement between theory, experiment and model. The simulated geometry consisted of a bilayer cantilever with length, width and thicknesses corresponding to the values discussed in Section 2.1. The material parameters used – Young's moduli, coefficients of thermal expansion, and Poisson's ratios – were the same ones used for obtaining the analytical results in Sections 3.1–3.3. All boundaries were free to move except one end of the cantilever, which was fixed. An initial strain of −0.256% was chosen, which produced the initial microactuator tip deflection of 67 μm observed experimentally at 21 °C. Since the VO$_2$ phase transition is a highly nonlinear hysteretic phenomenon, there are no preset parameters or functions that capture the behavior of VO$_2$ in the simulation software. To include this effect in the simulation, a nonlinear fit of the calculated strain as a function of temperature produced solely by the VO$_2$ transition was done through a nonlinear least square method of a modified Boltzmann model. For simplicity
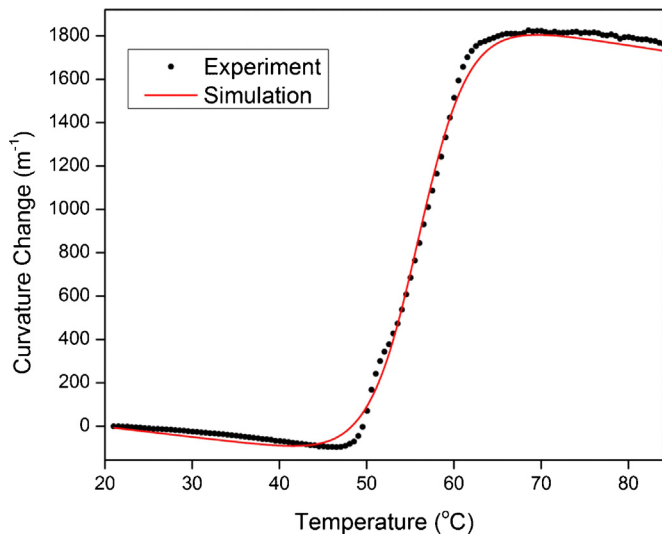

Fig. 9. Experimental (dots) and simulated (line) curvature change as a function of temperature.
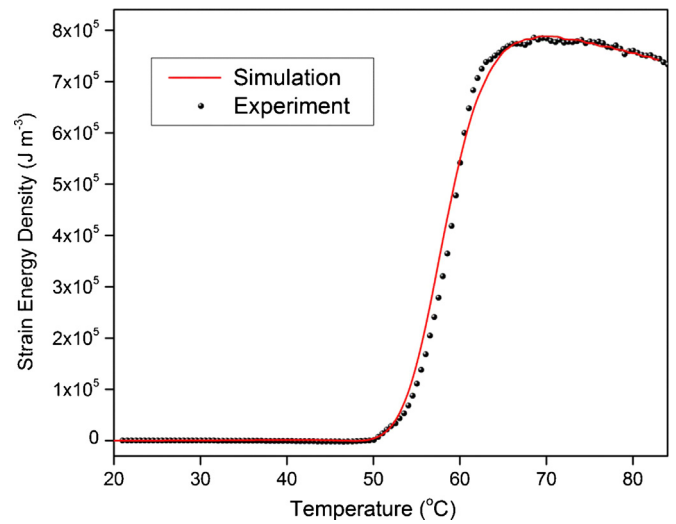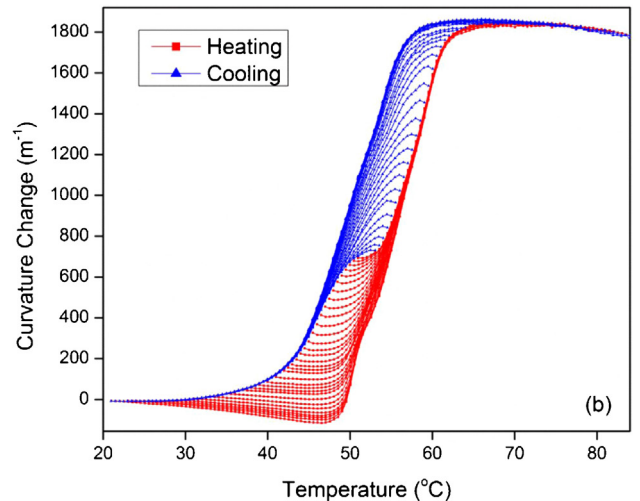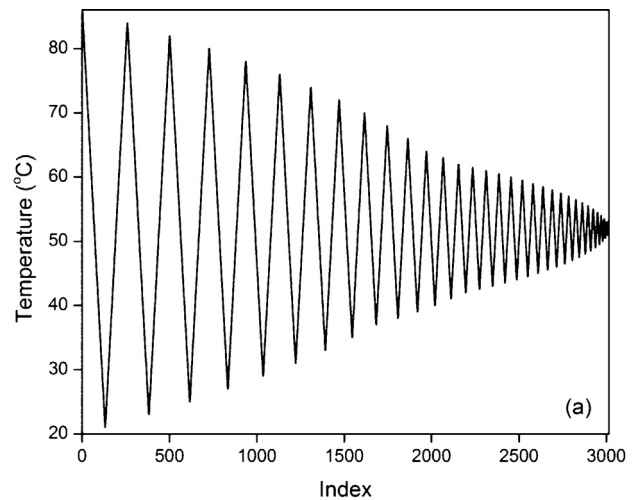

Fig. 11. Temperature sequences used for the hysteresis study (a) and experimental curvature measurements of the microactuator (b).
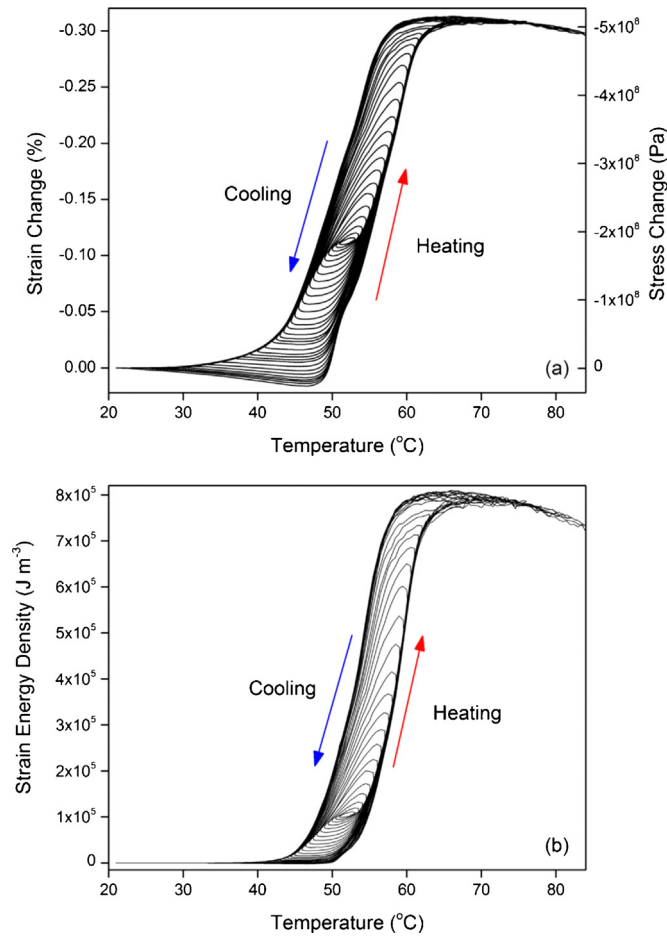
Fig. 12. Strain and stress (a), and strain energy density (b) evolution through the hysteresis.

is strikingly similar, corroborating the strain energy density values obtained experimentally.

3.5. Hysteresis evolution

The temperature sequence in Fig. 11a was used to generate the curvature change of the VO_2-coated microactuator shown in Fig. 11b. The inner loops in the curvature data are a memory effect from the highly hysteretic behavior of the VO_2 phase transition, which has also been observed in the electrical and optical properties of the material [39]. Although pronounced hysteresis is important for memory applications, it might hinder the development of microactuators due to sophisticated modeling and control it entails. In a recent work, the curvature change of a VO_2-coated microactuator was efficiently modeled with a modified Preisach operator and an inverse compensation technique was employed to control its curvature [40]. The evolution of properties throughout the hysteresis loop gives further insight into the performance and limitations of the microactuator. Fig. 12a shows the temperature dependent strain and stress changes obtained from Eqs. (2) and (3) using the curvature values in Fig. 11b and assuming a VO_2 biaxial modulus of 156 GPa. These measurements inside the hysteresis can be used to accurately predict the amount of stress/strain available in the device at a given temperature, the remaining stress/strain change achievable with an increase/decrease in temperature and, for a given temperature range, the range and the rate of change of the stress/strain. Fig. 12b shows the strain energy density of the microactuator, calculated with Eq. (5), through the device hysteresis loops measured. Here, the inside loop forms show a very different behavior than the stress/strain inner loops, which is mainly due to the squared relationship between strain energy density and microactuator curvature. The curves shown in Fig. 12a and b are relative to the initial value at 21 °C.

4. Conclusion

The curvature change of a VO_2-coated microactuator as a function of temperature was experimentally measured with a maximum value of approximately $1800\,m^{-1}$ through the material's phase transition. The curvature values were used to calculate the strain, stress and strain energy density of the microactuator. A maximum strain change of -0.32% and a recoverable stress of -510 MPa were obtained, which produced a maximum strain energy density of $8.1 \times 10^5\,J/m^3$. This strain energy was achieved in a temperature window of 15 °C. An excellent agreement was found between these experimentally obtained values and a finite element analysis simulation. The evolution of curvature, strain, stress and strain energy density across the hysteresis inner loops was also studied, revealing greater knowledge of the device performance.

purposes, only the strain major heating curve, shown in Fig. 5, was taken into consideration in the simulation and in the nonlinear fit. The strain produced only by the VO_2 transition was obtained by subtracting the thermal expansion terms from Eq. (2) such that

$$\varepsilon_{\phi T}(T) = \varepsilon_T(T) - (\alpha_f - \alpha_s)(T - T_{ref}), \tag{6}$$

where ε_T is the thermal strain, α is the thermal expansion coefficient, T is temperature in °C, and T_{ref} is the strain reference temperature (assumed to be 21 °C). The transition strain $\varepsilon_{\phi T}(T)$ was used to find the parameters of the model $\varepsilon_{\phi TS}(T)$ given by

$$\varepsilon_{\phi TS}(T) = \frac{a_1}{1 - \exp((T - a_2)/a_s)} + a_4 T^2 + a_S T + a_\varepsilon, \tag{7}$$

where $a_{1-\varepsilon}$ are the six model parameters (summarized in Fig. 8). As seen in Fig. 8, the model efficiently fits the experimental data with a coefficient of determination (R-squared) of 0.9998. Eq. (7) was included in the simulation as an axial strain, in the direction of the microactuator's length, on the VO_2 layer in the microactuator along with the thermal expansion effect of both layers. A temperature dependent study was performed where the temperature was monotonically increased from 21 to 84 °C uniformly through the cantilever length in steps of 0.5 °C. Fig. 9 shows the curvature change obtained from the simulation along with the experimental values. The simulated values clearly follow the experimental values, which validates the strain change obtained from the experimental data with Eq. (2). Fig. 10 shows the strain energy density obtained from the simulation and the experimentally obtained values as a function of temperature. The behavior between both curves

References

[1] J.A. Wright, T. Yu-Chong, C. Shih-Chia, A large-force, fully-integrated MEMS magnetic actuator, in: International Conference on Solid-State Sensors, Actuators and Microsystems, vol. 2, 1997, pp. 793–796.

[2] C.H. Ko, J.J. Yang, J.C. Chiou, Efficient magnetic microactuator with an enclosed magnetic core, Journal of Microlithography, Microfabrication and Microsystems 1 (2002) 144–149.
[3] J. Juuti, K. Kordas, R. Lonnakko, V.P. Moilanen, S. Leppavuori, Mechanically amplified large displacement piezoelectric actuators, Sensors and Actuators A: Physical 120 (2005) 225–231.
[4] R. Legtenberg, A.W. Groeneveld, M. Elwenspoek, Comb-drive actuators for large displacements, Journal of Micromechanics and Microengineering 6 (1996) 320–329.
[5] J.D. Grade, H. Jerman, T.W. Kenny, Design of large deflection electrostatic actuators, Journal of Microelectromechanical Systems 12 (2003) 335–343.
[6] E.J. García, J.J. Sniegowski, Surface micromachined microengine, Sensors and Actuators A: Physical 48 (1995) 203–214.
[7] D.J. Bell, T.J. Lu, N.A. Fleck, S.M. Spearing, MEMS actuators and sensors: observations on their performance and selection for purpose, Journal of Micromechanics and Microengineering 15 (2005) S153–S164.
[8] M. Mita, M. Arai, S. Tensaka, D. Kobayashi, H. Fujita, A micromachined impact microactuator driven by electrostatic force, Journal of Microelectromechanical Systems 12 (2003) 37–41.
[9] T. Akiyama, D. Collard, H. Fujita, Scratch drive actuator with mechanical links for self-assembly of three-dimensional MEMS, Journal of Microelectromechanical Systems 6 (1997) 10–17.
[10] B. Kim, M.G. Lee, Y.P. Lee, Y.I. Kim, G.H. Lee, An earthworm-like micro robot using shape memory alloy actuator, Sensors and Actuators A: Physical 125 (2006) 429–437.
[11] P. Krulevitch, A.P. Lee, P.B. Ramsey, J.C. Trevino, J. Hamilton, M.A. Northrup, Thin film shape memory alloy microactuators, Journal of Microelectromechanical Systems 5 (1996) 270–282.
[12] O.C. Jeong, S.S. Yang, Fabrication of a thermopneumatic microactuator with a corrugated p plus silicon diaphragm, Sensors and Actuators A: Physical 80 (2000) 62–67.
[13] J.W. Suh, C.W. Storment, G.T.A. Kovacs, Characterization of multi-segment organic thermal actuators, in: International Conference on Solid-State Sensors, Actuators and Microsystems, vol. 2, 1995, pp. 333–336.
[14] M.C. LeMieux, M.E. McConney, Y.H. Lin, S. Singamaneni, H. Jiang, T.J. Bunning, et al., Polymeric nanolayers as actuators for ultrasensitive thermal bimorphs, Nano Letters 6 (2006) 730–734.
[15] E.T. Enikov, S.S. Kedar, K.V. Lazarov, Analytical model for analysis and design of V-shaped thermal microactuators, Journal of Microelectromechanical Systems 14 (2005) 788–798.
[16] A. Atre, Analysis of out-of-plane thermal microactuators, Journal of Micromechanics and Microengineering 16 (2006) 205–213.
[17] G. Alici, V. Devaud, P. Renaud, G. Spinks, Conducting polymer microactuators operating in air, Journal of Micromechanics and Microengineering 19 (2009) 025017.
[18] Z. Chen, X. Tan, Monolithic fabrication of ionic polymer–metal composite actuators capable of complex deformation, Sensors and Actuators A: Physical 157 (2010) 246–257.
[19] B. Gaihre, G. Alici, G.M. Spinks, J.M. Cairney, Pushing the limits for microactuators based on electroactive polymers, Journal of Microelectromechanical Systems 21 (2012) 574–585.
[20] N.J. Conway, K. Sang-Gook, Large-strain, piezoelectric, in-plane micro-actuator, in: 17th IEEE International Conference on Micro Electro Mechanical Systems (MEMS), 2004, pp. 454–457.
[21] N.J. Graf, M.T. Bowser, A soft-polymer piezoelectric bimorph cantilever-actuated peristaltic micropump, Lab on a Chip 8 (2008) 1664–1670.
[22] A. Rúa, F.E. Fernández, N. Sepúlveda, Bending in VO$_2$-coated microcantilevers suitable for thermally activated actuators, Journal of Applied Physics 107 (2010) 074506.
[23] R. Cabrera, E. Merced, N. Dávila, F.E. Fernández, N. Sepúlveda, A multiple-state micro-mechanical programmable memory, Microelectronic Engineering 88 (2011) 3231–3234.
[24] E. Merced, N. Dávila, D. Torres, R. Cabrera, F.E. Fernández, N. Sepúlveda, Photo-thermal actuation of VO$_2$:Cr-coated microcantilevers in air and aqueous media, Smart Materials and Structures 21 (2012).
[25] R. Cabrera, E. Merced, N. Sepúlveda, F.E. Fernández, Dynamics of photothermally driven VO$_2$-coated microcantilevers, Journal of Applied Physics 110 (2011) 094510.
[26] A. Rúa, R. Cabrera, H. Coy, E. Merced, N. Sepúlveda, F.E. Fernández, Phase transition behavior in microcantilevers coated with M$_1$-phase VO$_2$ and M$_2$-phase VO$_2$:Cr thin films, Journal of Applied Physics 111 (2012) 104502.
[27] Y. Okada, Y. Tokumaru, Precise determination of lattice parameter and thermal expansion coefficient of silicon between 300 and 1500 K, Journal of Applied Physics 56 (1984) 314–320.
[28] D. Kucharczyk, T. Niklewski, Accurate X-ray determination of the lattice-parameters and the thermal-expansion coefficients of VO$_2$ near the transition-temperature, Journal of Applied Crystallography 12 (1979) 370–373.
[29] S. Timoshenko, Analysis of bi-metal thermostats, Journal of the Optical Society of America 11 (1925) 233–255.
[30] W.A. Brantley, Calculated elastic constants for stress problems associated with semiconductor devices, Journal of Applied Physics 44 (1973) 534–535.
[31] W. Fan, S. Huang, J. Cao, E. Ertekin, C. Barrett, D.R. Khanal, et al., Superelastic metal–insulator phase transition in single-crystal VO$_2$ nanobeams, Physical Review B 80 (2009) 241105.
[32] P. Jin, S. Nakao, S. Tanemura, T. Bell, L.S. Wielunski, M.V. Swain, Characterization of mechanical properties of VO$_2$ thin films on sapphire and silicon by ultra-microindentation, Thin Solid Films 343–344 (1999) 134–137.
[33] K.Y. Tsai, T.S. Chin, H.P.D. Shieh, Effect of grain curvature on nano-indentation measurements of thin films, Japanese Journal of Applied Physics 1 (43) (2004) 6268–6273.
[34] B. Viswanath, C.H. Ko, S. Ramanathan, Thermoelastic switching with controlled actuation in VO$_2$ thin films, Scripta Materialia 64 (2011) 490–493.
[35] S.D. Senturia, Microsystem Design, Kluwer Academic Publishers, 2001.
[36] A. Werber, H. Zappe, Thermo-pneumatically actuated, membrane-based micro-mirror devices, Journal of Micromechanics and Microengineering 16 (2006) 2524–2531.
[37] B. Yang, Q. Lin, A latchable microvalve using phase change of paraffin wax, Sensors and Actuators A: Physical 134 (2007) 194–200.
[38] N.D. Mankame, G.K. Ananthasuresh, Comprehensive thermal modelling and characterization of an electro-thermal-compliant microactuator, Journal of Micromechanics and Microengineering 11 (2001) 452–462.
[39] H. Coy, R. Cabrera, N. Sepúlveda, F.E. Fernández, Optoelectronic and all-optical multiple memory states in vanadium dioxide, Journal of Applied Physics 108 (2010) 113115.
[40] J. Zhang, E. Merced, N. Sepúlveda, X. Tan, Modeling and inverse compensation of non-monotonic hysteresis in VO$_2$-coated microactuators, IEEE/ASME Transactions on Mechatronics, http://dx.doi.org/10.1109/TMECH.2013.2250989

Biographies

Emmanuelle Merced received the BS and MS degrees in Electrical Engineering from the University of Puerto Rico at Mayagüez, Puerto Rico, in 2009 and 2011, respectively. He is currently working towards his PhD degree in the Department of Electrical and Computer Engineering, Michigan State University, United States. His current research interests include micro-actuators, self-sensing, smart material devices and mechatronics. He is a recipient of the NSF GRFP fellowship and was named Outstanding Student in 2013.

Xiaobo Tan received his BS and MS degrees in automatic control from Tsinghua University, Beijing, China, in 1995 and 1998, respectively, and his PhD in Electrical and Computer Engineering from the University of Maryland in 2002. He is currently an associate professor of Electrical and Computer Engineering and Mechanical Engineering at Michigan State University and director of the Smart Microsystems Laboratory. His research interests include electro-active polymer sensors and actuators, modeling and control of smart materials, underwater robotics, and adaptive autonomous cyber-physical systems.

Nelson Sepúlveda obtained his BS degree in Electrical and Computer Engineering from the University of Puerto Rico at Mayagüez in 2001, and his MS and PhD degrees in Electrical and Computer Engineering at Michigan State University, in 2002 and 2005, respectively. He is currently an assistant professor at Michigan State University and the director of the Applied Materials Group at this institution. His research interests are micro and nanometer-sized sensors and actuators, characterization of smart and multifunctional materials and their integration in microsystems.